



Research Article

Kinematic Calibration Based on the Multicollinearity Diagnosis of a 6-DOF Polishing Hybrid Robot Using a Laser Tracker

Dong Zhao ¹, Chenglin Dong,¹ Hao Guo,¹ and Wenjie Tian ²

¹Key Laboratory of Mechanism Theory and Equipment Design of the State Ministry of Education, Tianjin University, Tianjin, China

²School of Marine Science and Technology, Tianjin University, Tianjin, China

Correspondence should be addressed to Wenjie Tian; wenjietian@tju.edu.cn

Received 5 February 2018; Accepted 1 July 2018; Published 15 July 2018

Academic Editor: Massimiliano Ferrara

Copyright © 2018 Dong Zhao et al. This is an open access article distributed under the Creative Commons Attribution License, which permits unrestricted use, distribution, and reproduction in any medium, provided the original work is properly cited.

A general methodology for ensuring the geometric accuracy of a 6-DOF polishing hybrid robot having a 3UPS and UP parallel mechanism and a 3-DOF wrist is presented. The process is implemented in three steps: formulation of the error model containing complete source errors such as offset errors of the actuated joints and structural errors of the joints and links utilizing product of exponentials formula and screw theory. Measurement of the full pose error twist with a specially designed measurement tool having three reference points was undertaken. Identification of the source errors by a stepwise identification strategy to overcome the ill-conditioned problem arising from the multicollinearity and development of a linearized error compensator was completed. An experiment has been carried out on the prototype, and the results show that, after calibration, a position volumetric error of 0.07 mm and an orientation error of 0.07 degrees can be achieved over the cubic task workspace with repeatability of 0.016 mm and 0.010 degrees.

1. Introduction

The application of optical components has increased in recent years thanks to the rapid development of astronomy, space exploration, and high-end optical instruments. Computer Control Optimal Surfacing (CCOS) [1] is significant in optical component machining, which affects the material removal by controlling the dwell time and the pressure on the component surface; however, the high cost of a five-axis polishing machine tool restricts its large-scale application. Hybrid robots, as an alternative solution, which not only meet the requirements of accuracy and stability [2] but also are more cost-effective and flexible than polishing machine tools [3], have been used for many polishing processes [4–6].

As one of the most important performance specifications for industrial robots, geometric accuracy can be enhanced by kinematic calibration, which usually involves four steps: modelling, measurement, identification, and compensation [7, 8].

Error measurement in a robotic system has been investigated in many previous studies. The approaches can be classified into two categories: self-calibration or autonomous

calibration [9–11] and external calibration [12–14]. The former is implemented based on the sensors being placed on the active, passive, and/or redundant joint. Although this approach allows easy automatic calibration and online compensation, the installation of a large number of sensors increases the complexity of the system and its manufacturing cost. Therefore, this method is still very limited in application [15]. As a more common method, external calibration is carried out by minimizing the residual between the measured and nominal values of the robot end-effector with the aid of external pose sensors. Zhuang [16] and Vischer [17] used a theodolite and a 3D coordinate measuring machine to measure the full pose error of a robot, respectively; however, the measurement process is extremely complex, which leads to a reduction in practicability. Grosso [18] and Hager [19] presented a measurement scheme utilizing two cameras to capture a 3D image, which makes it difficult to meet the accuracy requirements of robot calibration. To complete the full pose error measurement in a simple way with less time cost, the most commonly used method is to measure three or more reference points fixed on the end-effector and then the pose error can be computed [20, 21]. For example, Nubiola [22]

proposed a measurement method using a single telescoping ball-bar and two fixtures and Nguyen [23] proposed another strategy based on a set of discrete points on a circular trajectory; however, the former has limitations on its measurement range and the number of measurable orientations, and the latter can only be applied to robots that have wholly revolute joints or ones in which only the last joint is revolute. Therefore an important issue to be solved in the kinematic calibration of hybrid robots is how to measure the full pose error in an economic way.

The kernel step in kinematic calibration is to identify complete source errors based on the measured pose errors, which is a parameter estimation problem in regression analysis. There have been many algorithms applied to robot calibration: the Levenberg-Marquardt (LM) method [24] is a classical nonlinear optimization algorithm that can effectively overcome the problem of the overparameterization and singularities. To overcome the deficiency in the LM method in which the convergence rate decreases if the search path is far from the optimal solution, a Trust Region (TR) method [25] is investigated to identify the source errors of the robot. Nevertheless, the number of iterations and optimization results of the nonlinear algorithm are significantly affected by the initial value, so the least square (LS) method [26, 27] based on the linear model is widely employed in practice because it is simpler and easier to use. The LS method can be directly adopted for the well-conditioned identification Jacobian; however, as the mechanical structure becomes more complex, more attention should be paid to deal with the ill-conditioned identification problem caused by multicollinearity between the source errors.

Driven by the practical need to ensure polishing accuracy, a general approach for kinematic calibration of the hybrid robot with “the parallel mechanism and 3-DOF wrist” structure is presented. The remainder of this paper is organized as follows: in Section 2, a linearized error model is formulated by product of exponentials and screw theory containing all source errors, which include offset errors in the actuated joints and structural errors in the joints and links. In Section 3, the pose error twists of the robot at different measurement configurations are computed using position data from three reference points on a special tool and the identification Jacobian is constructed. This is followed, in Section 4, by source error identification using a stepwise identification strategy based on multicollinearity diagnosis, which offers a more reliable estimation of source errors than the LS method when dealing with an ill-conditioned problem. Then, a linear error compensator is developed for real-time implementation. In Section 5, experiments are carried out on a prototype machine to verify the effectiveness of the proposed approach before conclusions are drawn in Section 6.

2. Error Modelling

Figure 1 shows 3D modelling of the hybrid robot, which is composed of a parallel mechanism, a wrist, and an end-effector. Only constrained by the nonactuated UP limb in the middle, the parallel mechanism with one-translational two-rotational (1T2R) DOF has the advantage of large position

workspace, which is actuated by three 6-DOF UPS limbs. Here, U, S, and P represent, respectively, universal, spherical, and prismatic joints, and the underlined P denotes an actuated prismatic joint. Considering that the position and orientation of the platform are dependent, a 3-DOF wrist is connected to the end of the platform to ensure the orientation capability of the end-effector, which constitutes the 6-DOF serial limb together with the parallel mechanism. As the end-effector is rigidly mounted at the end of the wrist, we treat the wrist and the end-effector as wrist for simplicity in the following. In this section, we will formulate the linear map between the pose error twist of the robot and all possible geometric source errors in joints and links.

To describe the source errors, the following frames are defined as shown in Figure 2: for convenience, we treat universal/spherical joints as two/three revolute joints having mutually orthogonal joint axes and number the UPS limbs as 1, 2, and 3 and the UP limb plus the wrist as limb 4. The base reference frame $\{R_0\}$ is located at the median point of the base, which also acts as the reference frame $\{R_{0,i}\}$ of limb i . Meanwhile, we place body fixed frames $\{R_{j,i}\}$ ($j = 1 \dots 6$) attached to the j th joint of limb i and place body fixed frames $\{R_{7,i}\}$ attached to the end-link of limb i . So, $\{R_{7,4}\}$ is the tool frame $\{R_t\}$. The aforementioned frames are all built by following the Denavit-Hartenberg (D-H) conventions with $A_{j,i}$ being the origin. Finally, we place floating frames $\{R'_{4,4}\}$ and $\{R'_0\}$ at point $A_{4,4}$ and P , respectively, with their three axes remaining parallel to those of $\{R_0\}$.

According to the structure characteristics of the hybrid robot, the following error modelling process can be divided into the parallel mechanism and the serial limb.

2.1. Error Modelling of the Parallel Mechanism. Based on the local POE (product of exponentials) formula method presented in [27], the homogeneous transformation matrix of $\{R_{j+1,i}\}$ with respect to $\{R_{j,i}\}$ can be expressed as

$$\mathbf{g}_{j+1,i}^j = \prod_{k=1}^6 \exp(\widehat{\xi}_{k,j,i} \zeta_{k,j,i}) \quad (1)$$

with

$$\begin{aligned} \exp(\widehat{\xi}_{k,j,i} \zeta_{k,j,i}) &= \mathbf{I}_4 + \widehat{\xi}_{k,j,i} \zeta_{k,j,i} + (1 - \cos \zeta_{k,j,i}) \widehat{\xi}_{k,j,i}^2 \\ &\quad + (\zeta_{k,j,i} - \sin \zeta_{k,j,i}) \widehat{\xi}_{k,j,i}^3 \end{aligned} \quad (2)$$

where $\widehat{\xi}_{k,j,i}$ ($k = 1, \dots, 6$) constitutes a basis of $se(3)$; $\zeta_{1,j,i}$, $\zeta_{2,j,i}$, and $\zeta_{3,j,i}$ ($\zeta_{4,j,i}$, $\zeta_{5,j,i}$, and $\zeta_{6,j,i}$) are the translations along (rotations about) $x_{j,i}$, $y_{j,i}$, and $z_{j,i}$, respectively.

Differentiating (1) with respect to $\{R'_{4,4}\}$ and applying appropriate adjoint transformation (for more details, see [27]), the pose error twist of $\{R_{j+1,i}\}$ can be made such that

$$\delta \rho_{j+1,i}^{4,4'} = \text{Ad}_{g_{j,i}^{4,4'}} \delta \zeta_{j,i} \quad (3)$$

with

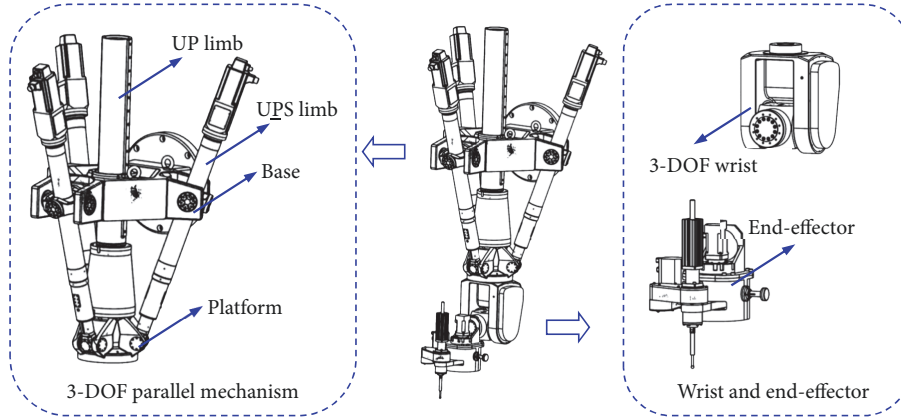


FIGURE 1: 3D modelling of the hybrid robot.

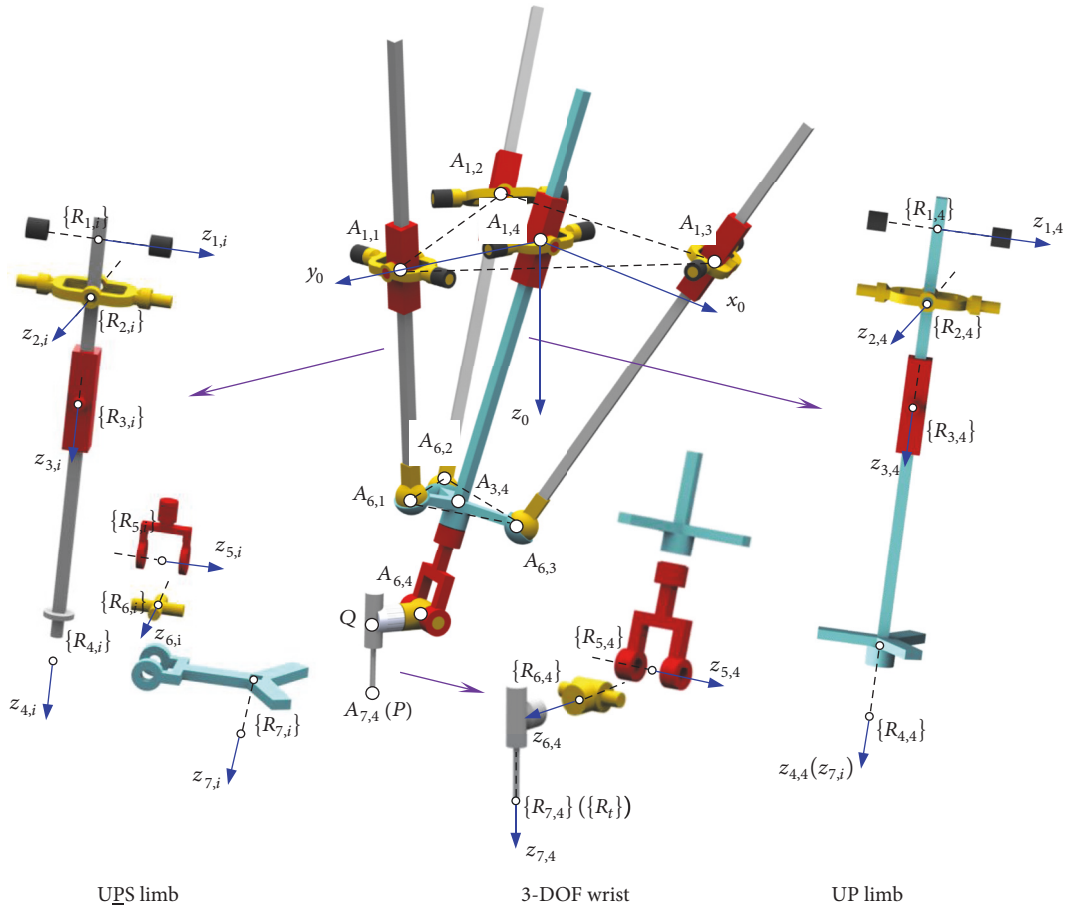


FIGURE 2: Schematic diagram and the frame establishment of the hybrid robot.

$$\text{Ad}_{g_{j,i}^{4,4'}} = \begin{bmatrix} \mathbf{R}_{j,i}^{4,4'} & [\mathbf{r}_{j,i}^{4,4'} \times] \mathbf{R}_{j,i}^{4,4'} \\ \mathbf{0}_{3 \times 3} & \mathbf{R}_{j,i}^{4,4'} \end{bmatrix} \quad (4)$$

$$\delta \zeta_{j,i} = (\delta \zeta_{1,j,i} \quad \delta \zeta_{2,j,i} \quad \delta \zeta_{3,j,i} \quad \delta \zeta_{4,j,i} \quad \delta \zeta_{5,j,i} \quad \delta \zeta_{6,j,i})^T$$

where $\mathbf{R}_{j,i}^{4,4'}$ is the orientation matrix of $\{R_{j,i}\}$ with respect to $\{R_{4,4}'\}$, $\mathbf{r}_{j,i}^{4,4'}$ is the vector from $A_{4,4}$ to $A_{j,i}$, and $[\mathbf{r}_{j,i}^{4,4'} \times]$ denotes the corresponding skew matrix; $\mathbf{0}_{3 \times 3}$ is a 3×3 zero matrix. It means that the source errors vector can be converted to

the error twist evaluated in $\{R'_{4,4}\}$ through the adjoint matrix transformation.

Based on (3), the pose error twist of all the limbs of the parallel mechanism evaluated in $\{R'_{4,4}\}$ can be developed directly such that

$$\delta \rho_i^{4,4'} = \sum_{j=0}^6 \text{Ad}_{g_{j,i}^{4,4'}} \delta \zeta_{j,i}, \quad i = 1, 2, 3 \quad (5)$$

$$\delta \rho_4^{4,4'} = \sum_{j=0}^3 \text{Ad}_{g_{j,4}^{4,4'}} \delta \zeta_{j,4} \quad (6)$$

Note that $\delta \zeta_{j,i}$ can be divided into a motion error along/about the j th joint axis and other errors except $\delta \zeta_{0,i}$, so (5) and (6) can be modified such that

$$\delta \rho_i^{4,4'} = \sum_{j=1}^6 \delta \zeta_{j,i} \xi_{ta,j,i} + \sum_{j=0}^6 \text{Ad}_{g_{j,i}^{4,4'}} \delta \zeta_{j,i}, \quad i = 1, 2, 3 \quad (7)$$

$$\delta \rho_4^{4,4'} = \sum_{j=1}^3 \delta \zeta_{j,4} \xi_{ta,j,4} + \sum_{j=0}^3 \text{Ad}_{g_{j,4}^{4,4'}} \delta \zeta_{j,4} \quad (8)$$

with

$$\delta \zeta_{j,i} = m^{j,i} \delta \zeta_{3,j,i} + (1-m)^{j,i} \delta \zeta_{6,j,i},$$

$$m = \begin{cases} 1 & \text{prismatic joint} \\ 0 & \text{rotation joint} \end{cases} \quad (9)$$

$$\delta \zeta_{j,i}$$

$$= (\delta \zeta_{1,j,i} \quad \delta \zeta_{2,j,i} \quad (1-m) \delta \zeta_{3,j,i} \quad \delta \zeta_{4,j,i} \quad \delta \zeta_{5,j,i} \quad m \delta \zeta_{6,j,i})^T$$

where $\xi_{ta,j,i}$ is the unit twist of the j th joint axis of limb i . Note that the UPS limbs and UP limb share the same platform, so

$$\delta \rho_P^{4,4'} = \delta \rho_i^{4,4'} = \delta \rho_4^{4,4'} \quad (10)$$

In order to generate the error model of the parallel mechanism, the motion errors of all the passive joints should be eliminated because they are dependent on the other source errors arising from the closed-loop structure of the parallel mechanism. With the help of the reciprocal screw theory [28], taking inner products on both sides of (7) with the unit wrench of actuators $\xi_{wa,3,i}$ and (8) with the unit wrench of constraints $\xi_{wc,j,c,4}$ and then rewriting them in matrix form yield

$$\begin{aligned} \delta \rho_P^{4,4'} &= \begin{bmatrix} J_{Pa} \\ J_{Pc} \end{bmatrix}^{-1} \left(\begin{pmatrix} \delta \zeta_{Pa} \\ \mathbf{0} \end{pmatrix} + \begin{bmatrix} G_{Pa} \\ G_{Pc} \end{bmatrix} \begin{pmatrix} \delta \zeta_{Pa} \\ \delta \zeta_{Pc} \end{pmatrix} \right) \\ &= J_P^{-1} \delta \zeta_P + J_P^{-1} G_P \delta \zeta_P \end{aligned} \quad (11)$$

with

$$J_{Pa} = [\xi_{wa,3,1} \quad \xi_{wa,3,2} \quad \xi_{wa,3,3}],$$

$$J_{Pc} = [\xi_{wc,1,4} \quad \xi_{wc,2,4} \quad \xi_{wc,3,4}]$$

$$G_{Pa} = \begin{bmatrix} \xi_{wa,3,1}^T \text{Ad}_1 & \mathbf{0} & \mathbf{0} \\ \mathbf{0} & \xi_{wa,3,2}^T \text{Ad}_2 & \mathbf{0} \\ \mathbf{0} & \mathbf{0} & \xi_{wa,3,3}^T \text{Ad}_3 \end{bmatrix},$$

$$G_{Pc} = \begin{pmatrix} \xi_{wc,1,4}^T \text{Ad}_4 \\ \xi_{wc,2,4}^T \text{Ad}_4 \\ \xi_{wc,3,4}^T \text{Ad}_4 \end{pmatrix}$$

$$\text{Ad}_i = [\text{Ad}_{g_{0,i}^{4,4'}} \quad \dots \quad \text{Ad}_{g_{6,i}^{4,4'}}], \quad (12)$$

$$\delta \zeta_{Pa} = (\delta \zeta_1^T \quad \delta \zeta_2^T \quad \delta \zeta_3^T)^T$$

$$\text{Ad}_4 = [\text{Ad}_{g_{0,4}^{4,4'}} \quad \dots \quad \text{Ad}_{g_{3,4}^{4,4'}}],$$

$$\delta \zeta_{Pc} = \delta \zeta_4$$

$$\delta \zeta_{Pa} = (\delta \zeta_{3,1} \quad \delta \zeta_{3,2} \quad \delta \zeta_{3,3})^T,$$

$$\delta \zeta_i = (\delta \zeta_{0,i}^T \quad \dots \quad \delta \zeta_{6,i}^T)^T,$$

$$\delta \zeta_4 = (\delta \zeta_{0,4}^T \quad \dots \quad \delta \zeta_{3,4}^T)^T$$

2.2. Error Modelling of the Serial Limb. On the basis of the method mentioned in the previous section, the pose error twist of the serial limb, which is composed of a "UP+RRR" kinematic chain, evaluated in $\{R'_0\}$ can be expressed as

$$\begin{aligned} \delta \rho &= \sum_{j=1}^6 \delta \zeta_{j,4} \xi_{ta,j,4} + \sum_{j=0}^6 \text{Ad}_{g_{j,4}^{0'}} \delta \zeta_{j,4} \\ &= \sum_{j=1}^3 \delta \zeta_{j,4} \xi_{ta,j,4} + \sum_{j=0}^3 \text{Ad}_{g_{j,4}^{0'}} \delta \zeta_{j,4} + \sum_{j=4}^6 \delta \zeta_{j,4} \xi_{ta,j,4} \\ &\quad + \sum_{j=4}^6 \text{Ad}_{g_{j,4}^{0'}} \delta \zeta_{j,4} \end{aligned} \quad (13)$$

Substituting (8) and (11) into (13) and rewriting in matrix form yield

$$\begin{aligned} \delta \rho &= \text{Ad}_{g_{4,4}^{0'}} \delta \rho_P^{4,4'} + J_S \delta \zeta_S + G_S \delta \zeta_S \\ &= \text{Ad}_{g_{4,4}^{0'}} J_P^{-1} \delta \zeta_P + \text{Ad}_{g_{4,4}^{0'}} J_P^{-1} G_P \delta \zeta_P + J_S \delta \zeta_S + G_S \delta \zeta_S \\ &= \mathbf{B} \delta \chi \end{aligned} \quad (14)$$

where

$$\begin{aligned}
\delta\chi &= \begin{pmatrix} \delta\varsigma \\ \delta\zeta \end{pmatrix}, \\
\delta\varsigma &= \begin{pmatrix} \delta\varsigma_p \\ \delta\varsigma_s \end{pmatrix}, \\
\delta\zeta &= \begin{pmatrix} \delta\zeta_p \\ \delta\zeta_s \end{pmatrix} \\
\mathbf{B} &= [\mathbf{J} \ \mathbf{G}], \\
\mathbf{J} &= [\text{Ad}_{g_{4,4}^{o'}} \mathbf{J}_P^{-1} \ \mathbf{J}_S], \\
\mathbf{G} &= [\text{Ad}_{g_{4,4}^{o'}} \mathbf{J}_P^{-1} \mathbf{G}_P \ \mathbf{G}_S] \\
\mathbf{J}_S &= [\xi_{ta,4,4} \ \xi_{ta,5,4} \ \xi_{ta,6,4}], \\
\mathbf{G}_S &= [\text{Ad}_{g_{4,4}^{o'}} \ \text{Ad}_{g_{5,4}^{o'}} \ \text{Ad}_{g_{6,4}^{o'}}] \\
\delta\varsigma_S &= (\delta\varsigma_{4,4} \ \delta\varsigma_{5,4} \ \delta\varsigma_{6,4})^T, \\
\delta\zeta_S &= (\delta\zeta_{4,4}^T \ \delta\zeta_{5,4}^T \ \delta\zeta_{6,4}^T)^T
\end{aligned} \tag{15}$$

3. Pose Error Twist Measurement

Since it is difficult to obtain all the source errors by direct measurement, parameter identification offers an effective way of obtaining them from pose error measurements. In this section, the focus is on the formulation of the identification Jacobian using position measurement.

Firstly, the workpiece frame $\{R_w\}$ is defined as the measurement frame (Figure 3). To facilitate computation, the measurement frame is then translated to the middle point of the task workspace, as the reference pose, where the nominal $z_{5,4}$ -axis is coincident with y -axis, and the nominal $z_{6,4}$ -axis is coincident with x -axis of $\{R_w\}$. Hence, the following adjoint transformation is made to obtain the pose error twist evaluated in $\{R_w\}$:

$$\delta\rho^w = \text{Ad}_{g_{o'}^w} \delta\rho^{o'} = \text{Ad}_{g_{o'}^w} \mathbf{B} \delta\chi \tag{16}$$

with

$$\begin{aligned}
\text{Ad}_{g_{o'}^w} &= \begin{bmatrix} {}^w\mathbf{R}_0 & \mathbf{0} \\ \mathbf{0} & {}^w\mathbf{R}_0 \end{bmatrix}, \\
{}^w\mathbf{R}_0 &= \text{Rot}\left(z, \frac{\pi}{2}\right) \text{Rot}\left(x, \pi - \gamma\right)
\end{aligned} \tag{17}$$

where $\delta\rho^{o'} = \delta\rho$ given in (14) and $\gamma = \pi/6$ is the nominal structural angle between z -axis and z_0 -axis. We still denote $\delta\rho^w$ as $\delta\rho$ and $\text{Ad}_{g_{o'}^w} \mathbf{B}$ as \mathbf{B} for simplicity below.

According to [29], the necessary conditions for $\delta\chi$ to be identifiable are as follows: (1) in the process of movement between measurement configurations, all of the actuated joints must be in motion; (2) the number of measurement

configurations $n \geq m/6$, where m is the number of irreducible source errors to be identified; (3) the six components of the pose error connected with each measurement configuration should be included.

The main difficulty of the above conditions is the pose error twist measurement because the orientation error cannot be measured directly. As shown in Figure 3, here, the pose error is developed with the aid of a special measurement tool, which is attached to the end-effector with three measurement points M_i ($i = 1, 2, 3$). Meanwhile, $\overline{M_2M_3}$ is ideally aligned with y -axis of $\{R_w\}$ at the reference pose.

To generate the orientation error in the k th measurement configuration, the plane formed by the measurement tool can be expressed as

$$a_k x + b_k y + c_k z = 1 \tag{18}$$

where a_k, b_k, c_k are unknown parameters. Considering all measurement points, (18) can be rewritten as

$$\mathbf{A}_k \mathbf{X}_k = \mathbf{L}_k \tag{19}$$

with

$$\begin{aligned}
\mathbf{A}_k &= \begin{bmatrix} x_{1,k} & y_{1,k} & z_{1,k} \\ x_{2,k} & y_{2,k} & z_{2,k} \\ x_{3,k} & y_{3,k} & z_{3,k} \end{bmatrix}, \\
\mathbf{X}_k &= \begin{pmatrix} a_k \\ b_k \\ c_k \end{pmatrix}, \\
\mathbf{L}_k &= \begin{pmatrix} 1 \\ 1 \\ 1 \end{pmatrix}
\end{aligned} \tag{20}$$

So the unknown parameters are determined from

$$\mathbf{X}_k = \mathbf{A}_k^{-1} \mathbf{L}_k \tag{21}$$

Then the rotation matrix of $\{R_{7,4}\}$ relative to $\{R_w\}$ at the k th measurement configuration can be defined by

$$\mathbf{R}_{m,k} = [\mathbf{n}_{1,k} \ \mathbf{n}_{2,k} \ \mathbf{n}_{3,k}] \tag{22}$$

where $\mathbf{n}_{1,k}, \mathbf{n}_{2,k}, \mathbf{n}_{3,k}$ are the unit vectors of the $x_{7,4}, y_{7,4}, z_{7,4}$ -axes evaluated in $\{R_w\}$, $\mathbf{n}_{3,k} = \mathbf{X}_k / \|\mathbf{X}_k\|_2$, $\mathbf{n}_{2,k} = (\mathbf{m}_{3,k} - \mathbf{m}_{2,k}) / \|(\mathbf{m}_{3,k} - \mathbf{m}_{2,k})\|_2$, and $\mathbf{n}_{1,k} = \mathbf{n}_{2,k} \times \mathbf{n}_{3,k}$. According to [12], the measured orientation $\theta_{m,k}$ can be easily obtained through $\mathbf{R}_{m,k}$ and the measured position $\mathbf{r}_{m,k} = (\mathbf{m}_{2,k} + \mathbf{m}_{3,k})/2$. The pose error twist of point M at the k th measurement configuration can be expressed as

$$\delta\rho_{m,k} = (\mathbf{r}_{m,k}^T \ \theta_{m,k}^T)^T - (\mathbf{r}_{c,k}^T \ \theta_{c,k}^T)^T \tag{23}$$

where $\mathbf{r}_{c,k}$ and $\theta_{c,k}$ denote the command position and orientation, respectively.

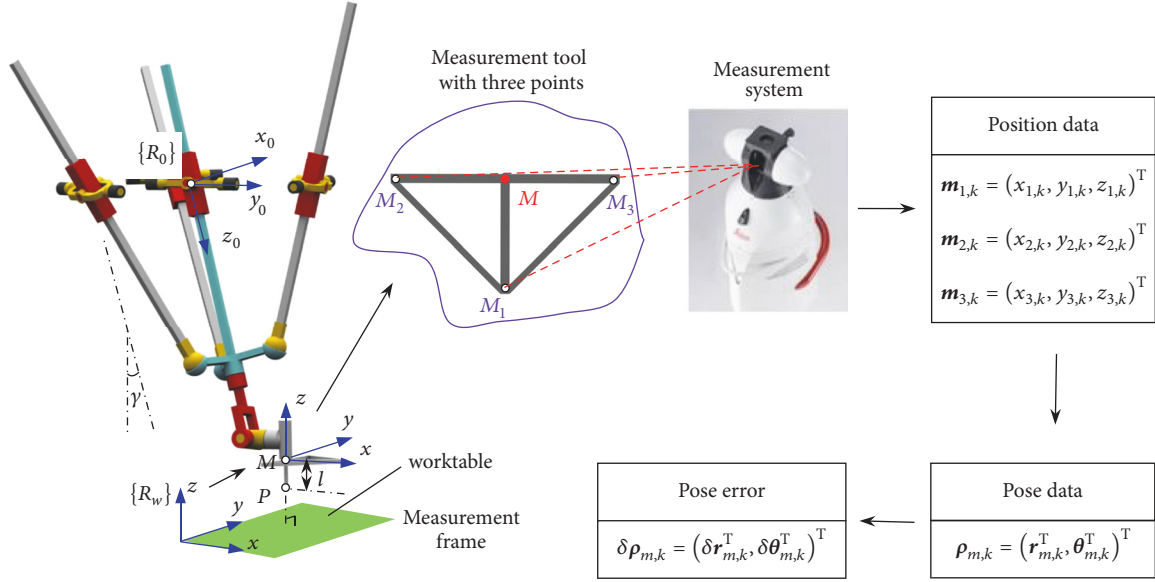


FIGURE 3: The method of the full pose error measurement.

Above all, the pose error twist of point P can be developed such that

$$\delta \boldsymbol{\rho}_k = \text{Ad}_{g_m'} \delta \boldsymbol{\rho}_{m,k} \quad (24)$$

with

$$\text{Ad}_{g_m'} = \begin{bmatrix} \mathbf{I}_3 & [\mathbf{p}_{M/P} \times] \\ \mathbf{0} & \mathbf{I}_3 \end{bmatrix} \quad (25)$$

where $\mathbf{p}_{M/P}$ is \overrightarrow{PM} evaluated in $\{R_w\}$ and $[\mathbf{p}_{M/P} \times]$ is the corresponding skew matrix of $\mathbf{p}_{M/P}$. It can be seen from (24) that this step should be carried out after kinematic calibration, so hereafter we will focus on the identification and compensation based on $\delta \boldsymbol{\rho}_{m,k}$. For convenience, we also denote $\delta \boldsymbol{\rho}_{m,k}$ as $\delta \boldsymbol{\rho}_k$.

Considering the entire measurement configurations, (16) can be rewritten as

$$\delta \mathbf{P} = \mathbf{H} \delta \boldsymbol{\chi} + \boldsymbol{\varepsilon} \quad (26)$$

with

$$\delta \mathbf{P} = \begin{pmatrix} \delta \boldsymbol{\rho}_1 \\ \delta \boldsymbol{\rho}_2 \\ \vdots \\ \delta \boldsymbol{\rho}_n \end{pmatrix}, \quad (27)$$

$$\mathbf{H} = \begin{pmatrix} \mathbf{B}_1 \\ \mathbf{B}_2 \\ \vdots \\ \mathbf{B}_n \end{pmatrix}$$

where \mathbf{H} denotes the identification Jacobian determined by the method of elementary transformations, $\delta \boldsymbol{\chi}$ denotes a corresponding set of irreducible source errors, $\boldsymbol{\varepsilon}$ is the noise satisfying the Gauss-Markov process, that is, $E(\boldsymbol{\varepsilon}) = 0$ and $\text{Cov}(\boldsymbol{\varepsilon}) = \sigma^2 \mathbf{I}_{6n}$, representing the expectation and covariance matrices of $\boldsymbol{\varepsilon}$.

4. Source Error Identification and Pose Error Compensation

In this section, a robust estimation algorithm for source errors identification will be investigated. Then, a linear error compensator is designed for real-time implementation.

4.1. Source Error Estimation Based on Multicollinearity Diagnosis. Although a set of linearly dependent source errors have been provided in (26), some approximate linear relationships, namely, multicollinearity, persist. At this point, the source error estimation produced by the LS method is no longer stable. It is difficult to satisfy the accuracy requirements of identification and calibration; therefore, a two-step estimation method is presented based on multicollinearity diagnosis to solve this problem.

Condition index and variance decomposition proportion (CIVDP) is a reliable way of diagnosing multicollinearity in the identification matrix, which not only can detect the number of multicollinearity relationships in $\delta \boldsymbol{\chi}$ but also can determine the source errors in $\delta \boldsymbol{\chi}$ and corresponding columns in \mathbf{H} .

Note that $\delta \boldsymbol{\chi}$ is composed of encoder offsets and structural errors of limb i , and \mathbf{H} can be divided into

$$\mathbf{H} = [\mathbf{J}' \quad \mathbf{G}'_1 \quad \mathbf{G}'_2 \quad \mathbf{G}'_3 \quad \mathbf{G}'_4] \quad (28)$$

where \mathbf{J}' is the matrix composed of columns corresponding to the encoder offsets and \mathbf{G}'_i is the matrix composed of columns

corresponding to the structural errors in limb i . The encoder offsets are the motion errors along/about actuated joint axes, so there is no multicollinearity in \mathbf{J}' . Then κ_j , the condition of \mathbf{J}' , can be treated as the criteria in condition index diagnosis. The condition index (CI) of \mathbf{G}'_i can be calculated by

$$\eta_{j,i} = \frac{\mu_{i,\max}}{\mu_{j,i}} \quad (29)$$

where $\mu_{i,\max}$ denotes the maximum singular value of \mathbf{G}'_i and $\mu_{j,i}$ denotes the j th singular value of \mathbf{G}'_i . The larger values of CI ($> 30\kappa_j$) indicate the number of multicollinearities in \mathbf{G}'_i [30].

The variance decomposition proportion (VDP) matrix $\mathbf{\Pi}_i$ of \mathbf{G}'_i , in which there is a multicollinearity relationship, can be further formulated such that

$$\pi_{jk,i} = \frac{(t_{kj,i}^2/\mu_{j,i}^2)}{\sum_{k=1}^p (t_{kj,i}^2/\mu_{j,i}^2)} \quad (30)$$

where $\pi_{jk,i}$ denotes the term (j, k) of $\mathbf{\Pi}_i$, $t_{kj,i}$ denotes the k th element in the j th eigenvector of $\mathbf{G}'_i{}^T \mathbf{G}'_i$, and p denotes the dimension of the eigenvector. It is interesting to find that the j th row of $\mathbf{\Pi}_i$ denotes the proportion of the variance in the source errors contributed by $\mu_{j,i}$. Finding the VDP value such that $\pi_{jk,i} > 0.5$ [30] means that the source errors in $\delta\chi$ and the columns in \mathbf{G}'_i can be sorted correspondingly: these are those columns affected by multicollinearity.

According to the multicollinearity diagnosis in $\delta\chi$, (26) can be rewritten as

$$\delta\mathbf{P} = [\mathbf{H}'_1 \ \mathbf{H}'_2] \begin{pmatrix} \delta\chi_1 \\ \delta\chi_2 \end{pmatrix} + \boldsymbol{\varepsilon} \quad (31)$$

where $\delta\chi_2$ ($\delta\chi_1$) is (not) affected by multicollinearity and \mathbf{H}'_2 (\mathbf{H}'_1) is the corresponding identification Jacobian, so the LS estimate of $\delta\chi$ can be expressed as

$$\delta\widehat{\chi} = \begin{pmatrix} \delta\widehat{\chi}_1 \\ \delta\widehat{\chi}_2 \end{pmatrix} = \begin{bmatrix} \mathbf{H}'_1{}^T \mathbf{H}'_1 & \mathbf{H}'_1{}^T \mathbf{H}'_2 \\ \mathbf{H}'_2{}^T \mathbf{H}'_1 & \mathbf{H}'_2{}^T \mathbf{H}'_2 \end{bmatrix}^{-1} \begin{bmatrix} \mathbf{H}'_1{}^T \\ \mathbf{H}'_2{}^T \end{bmatrix} \delta\mathbf{P} \quad (32)$$

where $\delta\widehat{\chi}_1$ ($\delta\widehat{\chi}_2$) is the LS estimate of $\delta\chi_1$ ($\delta\chi_2$). Although, during calculation, \mathbf{H}'_2 is used to generate $\delta\widehat{\chi}_1$, the stability of $\delta\widehat{\chi}_1$ is unaffected [31], so $\delta\widehat{\chi}_1$ can be used as a reliable estimate. For $\delta\widehat{\chi}_2$, the PCA (Principal Component Analysis) estimator is introduced to resolve the poor robustness problem caused by multicollinearity, which is an improved LS method that involves relinquishing the unbiased nature of the LS method to obtain a more reliable regression coefficient.

Taking $\delta\widehat{\chi}_1$ into (31) leads to

$$\delta\widehat{\mathbf{P}}_2 = \delta\mathbf{P} - \mathbf{H}'_1 \delta\widehat{\chi}_1 = \mathbf{H}'_2 \delta\chi_2 + \boldsymbol{\varepsilon} \quad (33)$$

According to [30], the PCA estimator of $\delta\chi_2$ is expressed as

$$\delta\widehat{\chi}_{2PCA} = \mathbf{V}_{PCA} \widehat{\boldsymbol{\beta}}_{PCA} \quad (34)$$

with

$$\widehat{\boldsymbol{\beta}}_{PCA} = (\mathbf{C}_{PCA}^T \mathbf{C}_{PCA})^{-1} \mathbf{C}_{PCA}^T \delta\widehat{\mathbf{P}}_2 \quad (35)$$

where \mathbf{C}_{PCA} denotes the matrix that is composed of the principle component in $\mathbf{C} = \mathbf{H}'_2 \mathbf{V}$ and \mathbf{V} is the matrix formed by the eigenvectors of $\mathbf{H}'_2{}^T \mathbf{H}'_2$ (for more details, see [30]). Finally, a reliable estimate of $\delta\chi$ can be developed such that

$$\delta\widehat{\chi} = (\delta\widehat{\chi}_1^T \ \delta\widehat{\chi}_{2PCA}^T)^T \quad (36)$$

4.2. Pose Error Compensation. Pose error compensation is the final step of the kinematic calibration. Once the source errors have been estimated, the pose error of the hybrid robot in the task workspace can be decreased with a linear error compensator by adjusting the command input of the actuated joint. Based on the above principle, (16) can be rewritten as

$$\delta\boldsymbol{\rho} = \mathbf{B} \delta\widehat{\chi} + \mathbf{J} \delta\boldsymbol{\zeta}_c \quad (37)$$

where $\delta\boldsymbol{\zeta}_c$ is the command input of actuated joints modified by the linear error compensator. A linear error compensator can be designed by forcing the pose error twist to be zero; namely, $\delta\boldsymbol{\rho} \equiv 0$. Hence, the modified command can be obtained such that

$$\delta\boldsymbol{\zeta}_c = -\mathbf{J}^{-1} \mathbf{B} \delta\widehat{\chi} \quad (38)$$

It is also important to note that some larger source errors make the error model nonlinear, so in practice compensation processing should be implemented in the Gauss-Newton iterative method until the compensation results converge. Based on the above description, Figure 4 shows the full procedures of the kinematic calibration of the 6-DOF polishing hybrid robot.

5. Experimental Validation

In this section, the multicollinearity diagnosis of all measurement configurations is implemented, and experiments are carried out on a prototype robot to validate the effectiveness of the proposed calibration method.

5.1. Multicollinearity Diagnosis. The task workspace of the hybrid robot is a 500mm \times 500mm \times 120mm cube and the nominal dimensions of the robot are given in Table 1. To fully reflect the multicollinearity of source errors in the whole task workspace, the measurement configurations are chosen as 36 points evenly distributed in each of the upper ($z = 60$ mm), middle ($z = 0$ mm), and lower ($z = -60$ mm) layers with respect to the reference orientation. In this way, all the actuated joints can be jointly driven and all position data can be measured by one installation of the reflector, which satisfies the requirements of identifiability and handleability at the same time.

Table 2 shows the 44 linear independent source errors in error model, including six encoder offsets of actuated joint, four structural errors of limb 1, six structural errors of limb 2, six structural errors of limb 3, and 22 structural

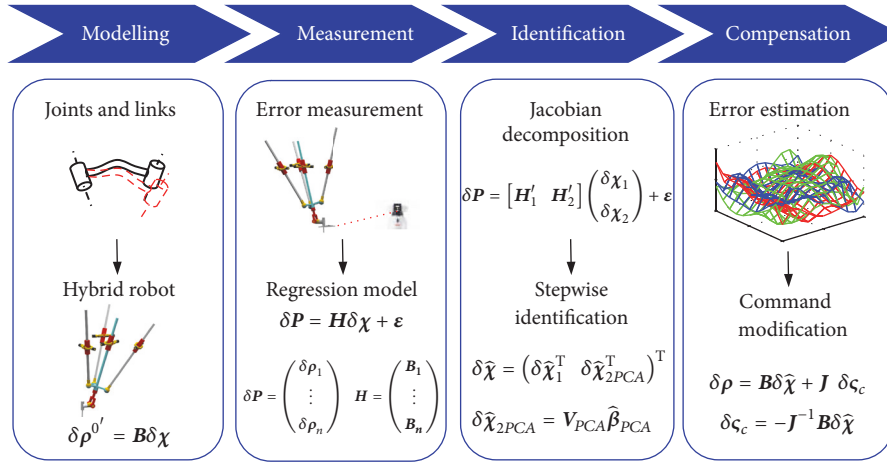


FIGURE 4: The flowchart of the kinematic calibration of the 6-DOF hybrid robot.

TABLE 1: Nominal geometric parameters of the hybrid robot (unit: mm).

$\overrightarrow{A_{0,i}A_{1,i}}$	$\overrightarrow{A_{3,4}A_{6,i}}$	$\overrightarrow{A_{3,4}A_{6,4}}$	$\overrightarrow{A_{6,4}Q}$	\overrightarrow{QM}
350	135	345	405	120

errors of limb 4. Then the CIs of G'_i are deduced (Table 3). Accordingly, there are five multicollinearity relationships in the structural errors of limb 4. It should be noted that Table 3 only lists the six larger CIs of G'_i , which are sufficient to determine the number of multicollinearity relationships, and there is no need to describe the remaining items. It is also interesting to see that limbs 2 and 3 have the same linear independent structural errors and CIs, because the two limbs, and the chosen measurement configurations, are all symmetrical about the layer $y = 0$.

The variance decomposition proportion matrix of limb 4 is further constructed to detect the multicollinearity relationship in $\delta \chi$. As shown in Table 4, it can be seen that there are five multicollinearity relationships existing, respectively, between (among) ${}^0\delta y_{1,4}$ and ${}^3\delta y_{4,4}$, ${}^0\delta x_{1,4}$ and ${}^2\delta z_{3,4}$, ${}^4\delta y_{5,4}$ and ${}^5\delta z_{6,4}$, ${}^0\delta z_{1,4}$, ${}^2\delta x_{3,4}$, and ${}^3\delta \beta_{4,4}$, ${}^4\delta x_{5,4}$, ${}^4\delta z_{5,4}$, ${}^4\delta \beta_{5,4}$, and ${}^6\delta x_{7,4}$. This means that the influence of a certain source error on the end-effector pose error can be deemed approximately equivalent to the linear superposition of the other source errors in the same multicollinearity relationship.

5.2. Experiment Implementation. To verify the effectiveness of the proposed method, kinematic calibration is carried out on a hybrid robot driven by an “IPC+PMAC” controller (Figure 5). According to the principle outlined in ISO 9283, the position volumetric error $|\delta \mathbf{r}|$ and the orientation volumetric error $|\delta \boldsymbol{\theta}|$ (simplified as position error and orientation error hereinafter) are taken as the evaluation standard of the pose error. A Leica AT901-LR laser tracker with a maximum observed deviation of 0.005 mm/m is used

to measure the position data of each reference point. Preliminary experiments show that the prototype robot has volumetric position repeatability of 0.016 mm and volumetric orientation repeatability of 0.010 degrees in the task workspace.

First, the workpiece frame is established with the aid of a square gauge mounted at a corner of the worktable (Figure 5). Then, the origin of the frame is translated to point M at the reference pose defined in Section 3, which is obtained with the aid of a laser tracker and mechanical means by driving the JOG motion of all of the actuated joints to the nominal required position. The pose error of a given measurement configuration evaluated in $\{R\}$ can thus be generated through the position data from three reference points, which is acquired by the laser tracker in the same measurement configuration.

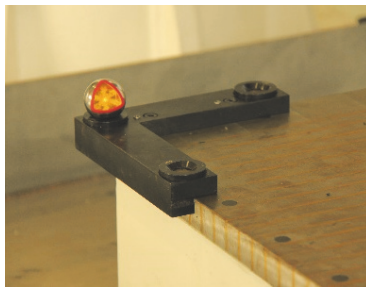
The experiment is carried out with the laser tracker according to the compensation strategy described in Section 4. To reduce the influence of thermal error, the hybrid robot is run for an hour to attain a relatively stable thermal state and the environmental temperature fluctuation is controlled to within $20.1 \pm 0.5^\circ\text{C}$ during the experiment. The measurement configurations are measured three times and then the mean values are substituted into future calculations. Figure 6 shows the pose errors of the workspace measured before calibration. It can be seen that the position error and orientation error are all approximately symmetric about x -axis and have the same regularity in their distribution. During the experiment, the modified command $\delta \zeta_c$ is determined by use of (38). After three “measurement-identification-compensation” looped iterations, the calibration comes to an end when the measured pose errors undergo no significant change before, and after, compensation. Comparing the data shown in Figures 6 and 7, the maximum position error is reduced from 6.886 mm to 0.065 mm and the maximum orientation error is reduced from 0.499 degrees to 0.069 degrees. The pose errors of the robot are thus effectively compensated.

TABLE 2: A set of linear independent source errors.

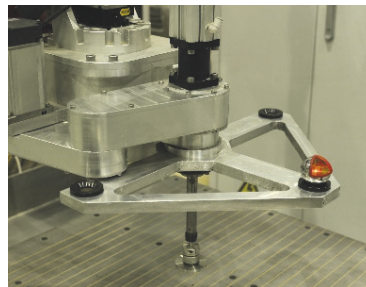
Limb	$\delta\zeta$	$\delta\zeta_{0,i}$	$\delta\zeta_{1,i}$	$\delta\zeta_{2,i}$
1	$\delta\zeta_{3,1}$	${}^0\delta x_{1,1}, {}^0\delta y_{1,1}, {}^0\delta z_{1,1}$	N/A	${}^2\delta x_{3,1}$
2	$\delta\zeta_{3,2}$	${}^0\delta x_{1,2}, {}^0\delta y_{1,2}, {}^0\delta z_{1,2}$	N/A	${}^2\delta x_{3,2}$
3	$\delta\zeta_{3,3}$	${}^0\delta x_{1,3}, {}^0\delta y_{1,3}, {}^0\delta z_{1,3}$	N/A	${}^2\delta x_{3,3}$
4	$\delta\zeta_{4,4}, \delta\zeta_{5,4}, \delta\zeta_{6,4}$	$\delta\zeta_{0,4}$	N/A	${}^2\delta x_{3,4}, {}^2\delta z_{3,4}, {}^2\delta\alpha_{3,4}$
Limb	$\delta\zeta_{3,i}$	$\delta\zeta_{4,i}$	$\delta\zeta_{5,i}$	$\delta\zeta_{6,i}$
1	N/A	N/A	N/A	N/A
2	N/A	N/A	N/A	${}^6\delta x_{7,2}, {}^6\delta z_{7,2}$
3	N/A	N/A	N/A	${}^6\delta x_{7,3}, {}^6\delta z_{7,3}$
4	${}^3\delta y_{4,4}, {}^3\delta\alpha_{4,4}, {}^3\delta\beta_{4,4}$	$\delta\zeta_{4,4}$	${}^5\delta x_{6,4}, {}^5\delta z_{6,4}, {}^5\delta\alpha_{6,4}$	${}^6\delta x_{7,4}, {}^6\delta\alpha_{7,4}$



(a)



(b)



(c)

FIGURE 5: The kinematic calibration experiment on a prototype robot. (a) The polishing hybrid robot, (b) workpiece frame establishment, and (c) position error measurement.

To evaluate the effectiveness of the kinematic calibration, extra measurements on the layers at $z = 30$ mm and $z = -30$ mm are taken. After calibration using the source errors listed in Table 5, the pose errors of the 36 points, evenly distributed in each of the two layers, are as listed in Table 6. It can be seen that the maximum position error and the maximum orientation error are 0.066 mm and 0.064 degrees,

respectively. These results further confirmed the effectiveness of the proposed method. It should be noted that, under the influence of the linear independent source errors and the biased estimation algorithm, the identified source errors cannot reflect the corresponding errors that exist in the prototype robot; however, they can still predict the pose errors of the robot effectively.

TABLE 3: Condition indices of G_i' .*

Limb	$\eta_{1,i}$	$\eta_{2,i}$	$\eta_{3,i}$	$\eta_{4,i}$	$\eta_{5,i}$	$\eta_{6,i}$
1	296.04	11.43	11.22	1	N/A	N/A
2	628.76	331.72	245.92	17.40	13.71	1
3	628.76	331.72	245.92	17.40	13.71	1
4	8.22×10^5	5.71×10^5	2.12×10^5	2.03×10^5	1.06×10^5	7.00×10^4

* indicates $\kappa_j = 2.35 \times 10^3$.

TABLE 4: Rows in Π_4 v: larger condition indices.

Larger CIs	${}^0\delta x_{1,4}$ (${}^3\delta\beta_{4,4}$)	${}^0\delta y_{1,4}$ (${}^4\delta x_{5,4}$)	${}^0\delta z_{1,4}$ (${}^4\delta y_{5,4}$)	${}^0\delta\alpha_{1,4}$ (${}^4\delta z_{5,4}$)	${}^0\delta\beta_{1,4}$ (${}^4\delta\alpha_{5,4}$)	${}^0\delta\gamma_{1,4}$ (${}^4\delta\beta_{5,4}$)	${}^2\delta x_{3,4}$ (${}^5\delta x_{6,4}$)	${}^2\delta z_{3,4}$ (${}^5\delta z_{6,4}$)	${}^2\delta\alpha_{3,4}$ (${}^5\delta\alpha_{6,4}$)	${}^3\delta y_{4,4}$ (${}^6\delta x_{7,4}$)	${}^3\delta\alpha_{4,4}$ (${}^6\delta\alpha_{7,4}$)
8.22×10^5	0 (0.01)	0.98 (0.11)	0.01 (0)	0.03 (0.31)	0 (0)	0 (0.23)	0.23 (0.05)	0 (0)	0 (0)	0.95 (0.32)	0 (0)
5.71×10^5	0.99 (0)	0 (0)	0 (0.01)	0 (0)	0.01 (0.04)	0.49 (0)	0 (0)	0.99 (0.02)	0.48 (0.03)	0 (0)	0.03 (0.01)
2.12×10^5	0 (0.87)	0.02 (0.20)	0.70 (0)	0.29 (0.01)	0 (0)	0 (0.05)	0.75 (0.28)	0 (0)	0 (0)	0.04 (0.01)	0 (0)
2.03×10^5	0.02 (0)	0 (0)	0 (0.98)	0 (0)	0.04 (0.02)	0.03 (0)	0 (0)	0 (0.98)	0.01 (0)	0 (0)	0.05 (0.17)
1.06×10^5	0 (0.04)	0.03 (0.61)	0.04 (0)	0.07 (0.62)	0 (0)	0 (0.65)	0.02 (0.49)	0 (0)	0 (0)	0 (0.63)	0 (0)

TABLE 5: Identified geometric source errors*.

$\xi_{3,1}$	$\xi_{3,2}$	$\xi_{3,3}$	$\xi_{4,4}$	$\xi_{5,4}$	$\xi_{6,4}$	${}^0\delta x_{1,1}$	${}^0\delta y_{1,1}$	${}^0\delta z_{1,1}$	${}^2\delta x_{3,1}$	${}^0\delta x_{1,2}$
3.139	-6.236	-15.964	0.020	0.005	-0.030	-6.152	1.932	1.325	-0.347	0.518
${}^0\delta y_{1,2}$	${}^0\delta z_{1,2}$	${}^2\delta x_{3,2}$	${}^6\delta x_{7,2}$	${}^6\delta z_{7,2}$	${}^0\delta x_{1,3}$	${}^0\delta y_{1,3}$	${}^0\delta z_{1,3}$	${}^2\delta x_{3,3}$	${}^6\delta x_{7,3}$	${}^6\delta z_{7,3}$
5.305	0.311	1.303	0.160	-0.106	-0.318	-2.714	0.201	-0.840	0.353	0.489
${}^0\delta x_{1,4}$	${}^0\delta y_{1,4}$	${}^0\delta z_{1,4}$	${}^0\delta\alpha_{1,4}$	${}^0\delta\beta_{1,4}$	${}^0\delta\gamma_{1,4}$	${}^2\delta x_{3,4}$	${}^2\delta z_{3,4}$	${}^2\delta\alpha_{3,4}$	${}^3\delta y_{4,4}$	${}^3\delta\alpha_{4,4}$
-0.019	-1.012	1.162	0.031	0.020	-0.065	5.067	0.020	-0.545	0.022	0.117
${}^3\delta\beta_{4,4}$	${}^4\delta x_{5,4}$	${}^4\delta y_{5,4}$	${}^4\delta z_{5,4}$	${}^4\delta\alpha_{5,4}$	${}^4\delta\beta_{5,4}$	${}^5\delta x_{6,4}$	${}^5\delta z_{6,4}$	${}^5\delta\alpha_{6,4}$	${}^6\delta x_{7,4}$	${}^6\delta\alpha_{7,4}$
0.075	0.301	-2.191	1.110	-0.062	0.027	-2.868	9.868	0.023	-0.531	1.143

* indicates length unit: mm and angle unit: degree

TABLE 6: Pose errors of the verification layers after fine calibration.

Pose error	Maximum value		Mean value	
	$z = 30$ mm	$z = -30$ mm	$z = 30$ mm	$z = -30$ mm
Position error (mm)	0.062	0.066	0.041	0.042
Orientation error (deg)	0.057	0.064	0.051	0.050

6. Conclusions

An approach to the kinematic calibration of a 6-DOF polishing hybrid robot was investigated and the following conclusions were drawn:

(1) The linearized error model of the hybrid robot was formulated by use of screw theory, and it contained the encoder offsets and all structural errors in the joints and links.

(2) A full pose error measurement approach for a polishing hybrid robot was proposed with the use of a special

measurement tool and a stepwise identification strategy was proposed to deal with the ill-conditioned problem caused by multicollinearity in the source errors.

(3) Experimental results obtained by use of the laser tracker showed that the pose error throughout the entire task workspace was improved significantly by use of the proposed approach. It remained to be seen how the calibration was related to practical optimal polishing and corresponding investigations are underway (at time of writing) based on the prototype robot.

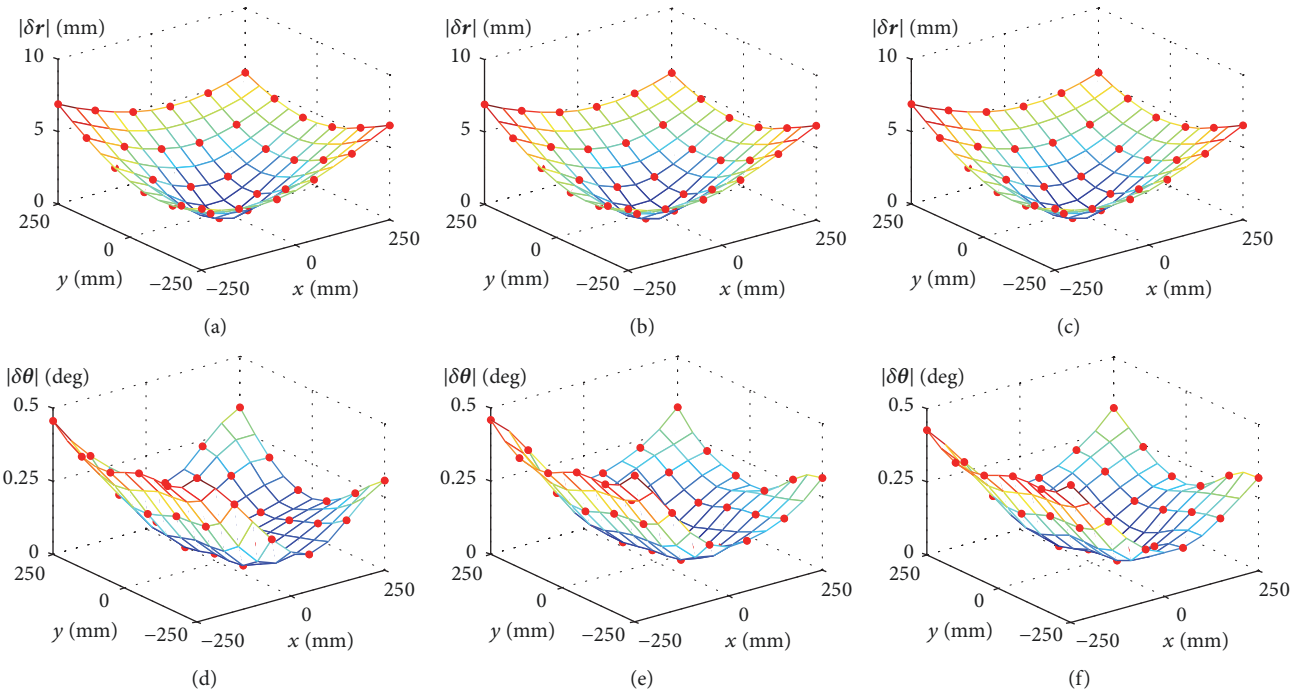


FIGURE 6: Error distributions before calibration of the workspace: position error: (a) in the upper layer, (b) in the middle layer, and (c) in the lower layer; orientation error: (d) in the upper layer, (e) in the middle layer, and (f) in the lower layer.

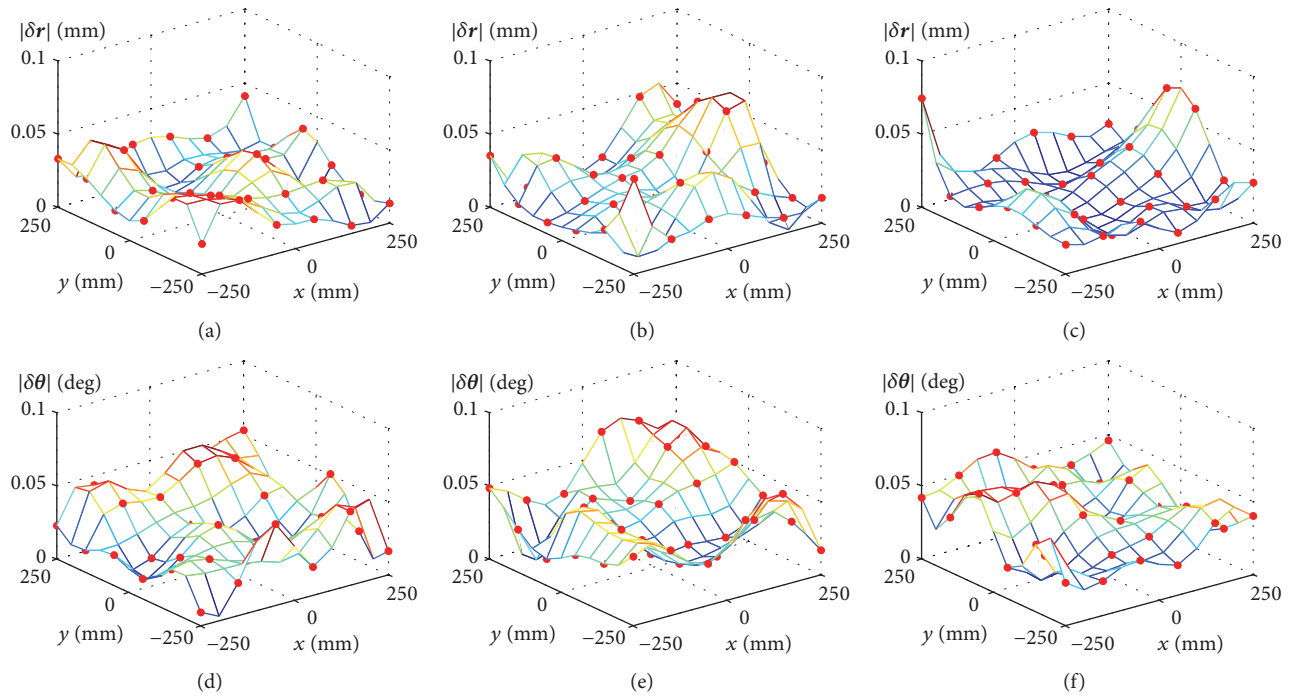


FIGURE 7: Error distributions after calibration of the workspace: position error: (a) in the upper layer, (b) in the middle layer, and (c) in the lower layer; orientation error: (d) in the upper layer, (e) in the middle layer, and (f) in the lower layer.

Data Availability

The authors declare that all relevant data within the paper are fully available without restriction.

Conflicts of Interest

The authors declare that there are no conflicts of interest.

Authors' Contributions

All authors contributed to the study presented in this manuscript. Dong Zhao established the error model and wrote the paper; Chenglin Dong and Dong Zhao designed the measurement tool; Dong Zhao and Hao Guo performed the experiment and analyzed the data. Wenjie Tian revised the paper and polished its language.

Acknowledgments

The authors acknowledge the support from the National Natural Science Foundation of China (NSFC) (Grants nos. 51605324, 51420105007, and 51605225) and EU H2020-MSCA-RISE Project (Grant no. 734272).

References

- [1] J. Wang, Y. Guo, and R. Zhu, "Research on robotic polishing of optic aspheric component," *Jiao Tong University*, vol. 49, pp. 636–639, 2010.
- [2] W. J. Rupp, "Conventional Optical Polishing Techniques," *Journal of Modern Optics*, vol. 18, no. 1, pp. 1–16, 1971.
- [3] M. Weck and D. Staimer, "Parallel kinematic machine tools - Current state and future potentials," *CIRP Annals - Manufacturing Technology*, vol. 51, no. 2, pp. 671–683, 2002.
- [4] Y. Kakinuma, K. Igarashi, S. Katsura, and T. Aoyama, "Development of 5-axis polishing machine capable of simultaneous trajectory, posture, and force control," *CIRP Annals - Manufacturing Technology*, vol. 62, no. 1, pp. 379–382, 2013.
- [5] C. Fan, G. Zhao, J. Zhao, L. Zhang, and L. Sun, "Calibration of a parallel mechanism in a serial-parallel polishing machine tool based on genetic algorithm," *The International Journal of Advanced Manufacturing Technology*, vol. 81, no. 1-4, pp. 27–37, 2015.
- [6] Z. Li, P. Xu, and J. Zhang, "Design of high-precision contour control system for a polishing mechanism," *Chinese Journal of Scientific Instrument*, vol. 36, pp. 330–337, 2015.
- [7] A. Traslosheros, J. M. Sebastián, J. Torrijos, R. Carelli, and E. Castillo, "An inexpensive method for kinematic calibration of a parallel robot by using one hand-held camera as main sensor," *Sensors*, vol. 13, no. 8, pp. 9941–9965, 2013.
- [8] Y. Zhao, Y. Cao, C. Zhang, D. Zhang, and J. Zhang, "Error Modeling and Experimental Study of a Flexible Joint 6-UPUR Parallel Six-Axis Force Sensor," *Sensors*, vol. 17, no. 10, pp. 2238–2258, 2017.
- [9] A. Joubair, L. F. Zhao, P. Bigras, and I. A. Bonev, "Use of a force-torque sensor for self-calibration of a 6-DOF medical robot," *Sensors*, vol. 16, no. 6, 2016.
- [10] H. Zhuang, "Self-calibration of parallel mechanisms with a case study on Stewart platforms," *IEEE Transactions on Robotics and Automation*, vol. 13, no. 3, pp. 387–397, 1997.
- [11] A. Elatta, L. Gen, and F. Zhi, "An Overview of Robot Calibration," *Information Technology Journal*, vol. 3, no. 1, pp. 74–78, 2004.
- [12] B. Liu, F. Zhang, X. Qu, and X. Shi, "A Rapid Coordinate Transformation Method Applied in Industrial Robot Calibration Based on Characteristic Line Coincidence," *Sensors*, vol. 16, no. 2, p. 239, 2016.
- [13] W. Tian, F. Yin, H. Liu et al., "Kinematic calibration of a 3-DOF spindle head using a double ball bar," *Mechanism and Machine Theory*, vol. 102, pp. 167–178, 2016.
- [14] P. Huang, J. Wang, and L. Wang, "Kinematic calibration of a hybrid machine tool with regularization method," *International Journal of Machine Tools and Manufacture*, vol. 51, pp. 210–220, 2011.
- [15] A. C. Majarena, J. Santolaria, D. Samper, and J. J. Aguilar, "An overview of kinematic and calibration models using internal/external sensors or constraints to improve the behavior of spatial parallel mechanisms," *Sensors*, vol. 10, no. 11, pp. 10256–10297, 2010.
- [16] H. Zhuang, O. Masory, and J. Yan, "Kinematic calibration of a Stewart platform using pose measurements obtained by a single theodolite," in *Proceedings of the 1995 IEEE/RSJ International Conference on Intelligent Robots and Systems. Part 3 (of 3)*, pp. 329–334, August 1995.
- [17] P. Vischer and R. Clavel, "Kinematic calibration of the parallel Delta robot," *Robotica*, vol. 16, no. 2, pp. 207–218, 1998.
- [18] E. Grosso, G. Metta, A. Oddera, and G. Sandini, "Robust visual servoing in 3-D reaching tasks," *IEEE Transactions on Robotics and Automation*, vol. 12, no. 5, pp. 732–742, 1996.
- [19] G. D. Hager, W.-C. Chang, and A. S. Morse, "Robot Hand-Eye Coordination Based on Stereo Vision," *IEEE Control Systems Magazine*, vol. 15, no. 1, pp. 30–39, 1995.
- [20] M. R. Driels, W. Swayze, and S. Potter, "Full-pose calibration of a robot manipulator using a coordinate-measuring machine," *The International Journal of Advanced Manufacturing Technology*, vol. 8, no. 1, pp. 34–41, 1993.
- [21] A. Omodei, G. Legnani, and R. Adamini, "Three methodologies for the calibration of industrial manipulators: Experimental results on a SCARA robot," *Journal of Robotic Systems*, vol. 17, no. 6, pp. 291–307, 2000.
- [22] A. Nubiola, M. Slamani, and I. A. Bonev, "A new method for measuring a large set of poses with a single telescoping ballbar," *Precision Engineering*, vol. 37, no. 2, pp. 451–460, 2013.
- [23] H.-N. Nguyen, J. Zhou, and H.-J. Kang, "A new full pose measurement method for robot calibration," *Sensors*, vol. 13, no. 7, pp. 9132–9147, 2013.
- [24] M. Grotjahn, M. Daemi, and B. Heimann, "Friction and rigid body identification of robot dynamics," *International Journal of Solids and Structures*, vol. 38, no. 10–13, pp. 1889–1902, 2001.
- [25] T. Messay, R. Ordóñez, and E. Marcil, "Computationally efficient and robust kinematic calibration methodologies and their application to industrial robots," *Robotics and Computer-Integrated Manufacturing*, vol. 37, article no. 1350, pp. 33–48, 2016.
- [26] R. He, Y. Zhao, S. Yang, and S. Yang, "Kinematic-parameter identification for serial-robot calibration based on POE formula," *IEEE Transactions on Robotics*, vol. 26, no. 3, pp. 411–423, 2010.

- [27] G. Chen, H. Wang, and Z. Lin, "Determination of the identifiable parameters in robot calibration based on the POE formula," *IEEE Transactions on Robotics*, vol. 30, no. 5, pp. 1066–1077, 2014.
- [28] H. Liu, T. Huang, and D. G. Chetwynd, "A General Approach for Geometric Error Modeling of Lower Mobility Parallel Manipulators," *Journal of Mechanisms and Robotics*, vol. 3, no. 2, p. 021013, 2011.
- [29] T. Huang, D. G. Chetwynd, D. J. Whitehouse, and J. Wang, "A general and novel approach for parameter identification of 6-DOF parallel kinematic machines," *Mechanism and Machine Theory*, vol. 40, no. 2, pp. 219–239, 2005.
- [30] C. Douglas, A. Elizabeth, and V. Geoffrey, *Introduction to linear regression analysis*, Wiley, New Jersey, USA, 2011.
- [31] L. Zhang, Y. Gu, and Q. Gui, "Biased estimator based on diagnosis and measure of multicollinearity," *Journal of Geodynamics*, vol. 27, pp. 99–102, 2007.



Hindawi

Submit your manuscripts at
www.hindawi.com

